

Radiative decay of muonic molecules in resonance states

Takuma Yamashita*

*Institute for Excellence in Higher Education, Tohoku University, Sendai 980-8576, Japan and
Department of Chemistry, Tohoku University, Sendai, 980-8578, Japan*

Kazuhiro Yasuda and Yasushi Kino

Department of Chemistry, Tohoku University, Sendai, 980-8578, Japan

(Dated: July 3, 2024)

In this study, we theoretically investigated x-ray spectra from the radiative decay of muonic deuterium molecules $dd\mu$ in resonance states which plays an important role in a new kinetic model of muon catalyzed fusion (μ CF). The resonance states are Feshbach resonances located below the $d\mu(n=2) + d$ threshold energy and radiatively decay into the continuum or bound states. The x-ray spectra having characteristic shapes according to the radial distribution of the two nuclei are obtained using precise three-body wave functions. We carefully examined the convergence of the x-ray spectra and achieved agreements between the length- and velocity-gauge calculations. We revealed a non-adiabatic kinetic energy distribution of the decay fragments, indicating that the radiative decay results in epithermal muonic atoms. We also investigated the decay branch directly resulting in bound-state muonic molecules. Some resonance states $dd\mu^*$ and $dt\mu^*$ are found to have high branching ratios to the bound state where intramolecular nuclear fusion occurs. The direct formation of the muonic molecules in the bound states from metastable muonic atoms can be a fast track in the μ CF cycle which skips slow path to form the bound state from the ground-state muonic atoms and increases the μ CF cycle rate. Although the spectra from the radiative decays are located in the energy range of 1.5–1.997 keV, close to the $K\alpha$ x-ray of 1.997 keV from muonic hydrogen atoms, recently developed state-of-the-art microcalorimeters can distinguish them.

I. INTRODUCTION

A muon (μ), an elementary particle with a mass 207 times greater than that of an electron, forms a compact molecule with two hydrogen nuclei. When the nuclei are deuteron or triton, nuclear fusion occurs in the muonic hydrogen molecules, i.e., $dd\mu$, $dt\mu$, and $tt\mu$. The muon is released after the intramolecular nuclear fusion repeatedly causes the nuclear fusion reactions in hydrogen targets during its lifetime of 2.2 μ s, which is so called muon catalyzed fusion (μ CF) [1–4] and the cyclic process is called μ CF cycle. For applications of the μ CF, it is necessary to increase the cycle rate by elucidating the elementary processes of the muonic atoms in the hydrogen.

The muonic hydrogen atom is initially formed in a highly excited state and subsequently cascades to lower levels [5]. One of the crucial problems in cascade processes is the dynamics involving the metastable state of the muonic hydrogen atom, i.e., the $2s$ state, which has been investigated both theoretically [6–12] and experimentally by laser spectroscopy [13–16].

The metastable state of a muonic hydrogen atom $d\mu(2s)$ can produce a muonic molecule in the resonance states as follows.

$$d\mu(2s) + D_2(\mathcal{L}_i, v_i) \rightarrow [(dd\mu^*)dee](\mathcal{L}_f, v_f), \quad (1)$$

where $d\mu$ denotes the muonic deuterium atom, and $\mathcal{L}_{i/f}, v_{i/f}$ are the rotational and vibrational quantum

numbers of the initial/final states, respectively. $dd\mu^*$ denotes a muonic deuterium molecule $dd\mu$ in a resonance state, in which the muonic molecular orbital is excited. The final-state molecule $[(dd\mu^*)dee]$ is a complex system in which $dd\mu^*$ behaves as a quasi-nucleus, and the two electrons bind the two nuclei $dd\mu^*$ and d . The reaction (1) was proposed as an analogy of the $dd\mu$ formation mechanism, called a Vesman mechanism [17], which is presented as follows:

$$d\mu(1s) + D_2(\mathcal{L}_i, v_i) \rightarrow [(dd\mu)dee](\mathcal{L}_f, v_f). \quad (2)$$

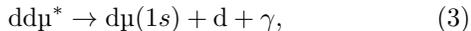
The excess energy, i.e., the sum of the binding energy of $dd\mu$ (~ 1.97 eV) and collision energy, is resonantly transferred to the rovibrational excitation energy of the two nuclei in the $[(dd\mu)dee]$ molecule. Because the resonance states of the muonic molecules $dd\mu^*$ are supported by long-range ion-dipole interactions between an excited muonic atom and the nucleus, the energy levels of $dd\mu^*$ accumulate below the dissociation limit, thus providing a denser level density and more suitable conditions for the Vesman mechanism. Therefore, the formation rate of the resonance states of muonic molecules is estimated to be significantly higher than that of $dd\mu$ [6–8].

The fate of the $2s$ state of the muonic atom has involved a puzzle. It is known that the quenching rate of the $2s$ state of the muonic atom ($p\mu$ in the H_2 target and $d\mu$ in the D_2 target) is smaller than that predicted by a conventional cascade model [15]. As the formation of a resonant muonic molecule quenches the $2s$ state of the muonic atom, the reaction (1) can be a mechanism to explain the observed population of the $2s$ state of the muonic atoms. Furthermore, deexcitation

* tyamashita@tohoku.ac.jp

processes via $d\mu^*$ in the D_2/T_2 mixture target increase $d\mu(1s)$ population and can explain the observed μCF cycle rate [6, 8, 12]. However, a cascade model has recently been developed [9–11] that indicates the importance of the direct Coulomb decay and collision-induced radiative quenching, which explains the observed population of $p\mu(2s)$ and $d\mu(2s)$ without assuming the reaction (1).

In this study, we calculate the x-ray spectra of the radiative decay of the resonance states $dd\mu^*$ into the continuum state,



or to a bound state,



The process (3) produces x-rays with characteristic energy profiles depending on their rotational and vibrational states [18, 19] in the energy range of 1.5–1.997 keV. The x-ray spectra, therefore, are footprints indicating the presence of these molecules. Thus far, it has been difficult to distinguish this broad x-ray spectrum from monoenergetic K_α x-rays of muonic atoms (1.997 keV) because of the energy resolution of the detectors. Recently, high-resolution x-ray spectroscopy with microcalorimeters has been successfully applied to determine the energy levels of muonic atoms [20–22] and show sufficient performance for x-ray energy of several keV with FWHM of 6 eV. The x-ray spectra from $dd\mu^*$ obtained via the process (3) were theoretically reported in previous studies [18, 19] for several states. To analyze the forthcoming experiments, as $dd\mu^*$ is expected to form in various rotational and vibrational states, more comprehensive spectrum information is required. Furthermore, the x-ray intensity from the process (4) has not been previously investigated; however, this process (4) could introduce a direct pathway to the bound state and produce monoenergetic x-rays that differ from the K_α x-rays. Thus, in this study, we investigate the radiative decay of muonic molecules in the resonance states and predict the x-ray spectra from the rotational states of $J = 0-3$ and vibrational states of $v = 0-8$. We solve the Schrödinger equation for a three-body system using the Gaussian expansion method [23] after separation of the center-of-mass motion. The transition rates are calculated using the complex scaling method under the dipole approximation.

The remainder of this paper is organized as follows. Sec. II outlines the theoretical calculations. Sec. III presents the x-ray spectra of each resonance state, angular momentum dependency of the x-ray spectra, and resonance-bound transition rates. Sec. IV summarizes the discussion. Atomic units (a.u.; $m_e = \hbar = e = 1$) and muonic atomic units (m.a.u.; $m_\mu = \hbar = e = 1$) are used throughout this paper, except when specified otherwise.

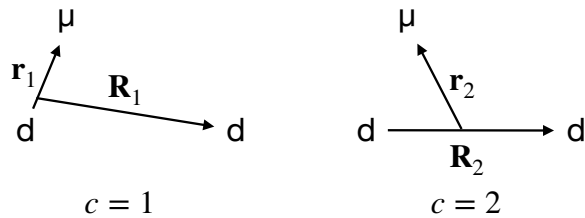


FIG. 1. Jacobi coordinate systems used in this study.

II. THEORY

A. Complex coordinate rotation method for three-body systems

We consider the three-body Hamiltonian involving kinetic energy operators (separated from the motion of the center of mass) and the Coulomb potential energy operators:

$$\hat{H} = \sum_{i=1}^3 -\frac{1}{2m_i} \nabla_{r_i}^2 + \frac{1}{2m_G} \nabla_{r_G}^2 + \frac{1}{r_{12}} - \frac{1}{r_{13}} - \frac{1}{r_{23}}, \quad (5)$$

where m_i is the mass of particle i ($i = 1: d, i = 2: d$, and $i = 3: \mu$), m_G is the mass of the system, ∇_{r_i} is a differential operator for the position vector \mathbf{r}_i , ∇_{r_G} is a differential operator for the center of mass, and r_{ij} is the relative distance between the particles i and j . We use the deuteron-muon mass ratio $m_d/m_\mu = 17.75167454$ [24] for comparison with the previous study [19]. The muon-electron mass ratio $m_\mu/m_e = 206.768283$ [25] is used throughout this work.

We adopt a complex coordinate rotation (CCR) method to calculate the resonance states and their radiative decays. A CCR Hamiltonian $H(\theta)$ is formally written as

$$H(\theta) = R(\theta)HR(-\theta), \quad (6)$$

where $R(\theta) = \exp[-\theta(\mathbf{r} \cdot \mathbf{p} + \mathbf{p} \cdot \mathbf{r})/2]$ is the complex rotation operator. $H(\theta)$ corresponds to the Hamiltonian where the distance r is scaled by a complex factor of $e^{i\theta}$ as $r \rightarrow re^{i\theta}$.

The eigen functions $\psi_{J,v}(\theta)$ of $H(\theta)$ are expanded in terms of L^2 integrable basis functions and obtained by solving the generalized complex eigenvalue problem,

$$\langle \bar{\psi}_{J,v'}(\theta) | H(\theta) | \psi_{J,v}(\theta) \rangle = E_{J,v}(\theta) \delta_{v'v}, \quad (7)$$

where J is the total orbital angular momentum quantum number, $v = 1, \dots$ denotes the index of the eigenstates, and $\bar{\psi}_{J,v}(\theta)$ denotes the complex conjugate of $\psi_{J,v}(\theta)$, with the exception of the angular part. For resonance states, the complex eigenvalues obtained by the CCR method take stationary values at $\theta = \theta'$ on the complex

energy plane, with the real part providing the resonance energy $E_{J,v}^{(R)}$ and the imaginary part Γ providing the resonance width:

$$E_{J,v}(\theta') = E_{J,v}^{(R)} - i\Gamma/2. \quad (8)$$

For continuum states, they exist on a line rotated by $-\theta$ from the real axis, centered around the threshold energy E_{th} :

$$E_{J,v}(\theta) \simeq E_{\text{th}} + K_{\text{rel}}(\cos 2\theta - i \sin 2\theta), \quad (9)$$

where K_{rel} denotes the kinetic energy of relative motion of the fragments.

The wave function $\psi_{J,v}(\theta)$ is expressed as

$$\begin{aligned} \psi_{J,v}(\theta) = & \sum_{c=1}^2 \sum_{l_{ci}, L_{cj}} \sum_{ij} (1 \pm P_{\text{dd}}) \\ & \times \left\{ C_{cijl_{ci}L_{cj}}^{(v)}(\theta) r_c^{l_{ci}} R_c^{L_{cj}} \exp(-a_i r_c^2 - A_j R_c^2) \sin(\beta A_j R_c^2) \right. \\ & \left. + D_{cijl_{ci}L_{cj}}^{(v)}(\theta) r_c^{l_{ci}} R_c^{L_{cj}} \exp(-a_i r_c^2 - A_j R_c^2) \cos(\beta A_j R_c^2) \right\} \\ & \times \left[Y_{l_{ci}}(\hat{\mathbf{r}}_c) \otimes Y_{L_{cj}}(\hat{\mathbf{R}}_c) \right]_{JM}, \quad (10) \end{aligned}$$

where M denotes a projection of the total angular momentum J onto the z -axis. c denotes the coordinate system specified by $\{\mathbf{r}_c, \mathbf{R}_c\}$ (Fig. 1); P_{dd} is a permutation operator for two identical deuterons; a_i , A_j , and β are real numbers; i denotes an imaginary unit; and $Y_{l_{ci}}(L_{cj})$ denotes the spherical harmonics of angular momentum quantum number $l_{ci}(L_{cj})$. $[\dots]$ denotes a tensor product of two angular momentum states given by the linear combination of spherical harmonics with Clebsch–Gordan coefficients as defined in Ref. [26]. The $\beta \neq 0$ introduces oscillating Gaussian functions [23]. These basis functions are suitable for describing the vibrationally excited state, the inter-nuclear wave function of which increases the number of nodes. In this study, we set $\beta = 1.5$.

As the deuteron has spin 1, the total wave function including the spin part must be symmetric against the permutation of the two d nuclei. When the two d nuclei configure the total nuclear spin $S_{\text{nucl}} = 0$ or 2, the spin part is symmetric; however, in the $S_{\text{nucl}} = 1$ case, the spin part is antisymmetric against the permutation of the two deuterons. Thus, we select $(1 + P_{\text{dd}})$ for $S_{\text{nucl}} = 0$ and 2 and $(1 - P_{\text{dd}})$ for $S_{\text{nucl}} = 1$. The spatial parity of the wave function is determined by $\Pi = (-1)^{l_{ci} + L_{cj}}$. Hereafter, we distinguish the symmetry of the dd μ states by the total nuclear spin S , total orbital angular momentum quantum number J , and the spatial parity Π (*even* or *odd*) and denote the symmetry as ${}^{2S_{\text{nucl}}+1}J^{e/o}$.

The convergence with respect to the number of angular momenta l_{ci} and L_{cj} when using the two coordinate systems is much faster than using a single coordinate system. The basis functions written in $c = 1$ and $c = 2$ are suited for the description of the d μ -d interaction and muonic molecular orbital around two deuterons, respectively. The linear coefficients $C_{cijl_{ci}L_{cj}}^{(v)}(\theta)$ and

$D_{cijl_{ci}L_{cj}}^{(v)}(\theta)$ which are complex values depending on θ are determined such that the $H(\theta)$ is diagonalized as Eq. (7). Hereafter, we denote the total number of basis functions, namely the number of linear coefficients, by N_{max} .

B. Calculation of resonance-continuum x-ray spectrum

We calculate the radiative decay rates of the dd μ^* in the rovibrational state (J, v_r) where v_r denotes the vibrational quantum number. The energy derivative of the radiative decay rate of the resonance state into a continuum state, $d\Gamma_{\text{RC}}/dE_\gamma$, can be calculated by dipole approximation as

$$\frac{d\Gamma_{\text{RC}}}{dE_\gamma} = \frac{4}{3} \alpha^3 E_\gamma^3 |\langle \Psi_{\text{C}}(E_f) | \mathbf{d} | \Psi_{\text{R}} \rangle|^2, \quad (11)$$

where Ψ_{R} is a wave function of the resonance state, and Ψ_{C} is an energy-normalized continuum wave function corresponding to the energy E_f . E_γ denotes the x-ray energy, α is the fine structure constant, and \mathbf{d} denotes the electric dipole moment operator. The energy of the continuum state E_f satisfies

$$E_f = E_{J,v_r}^{(R)} - E_\gamma \quad (12)$$

where $E_{J,v_r}^{(R)}$ is the resonance energy of dd μ^* .

The $d\Gamma_{\text{RC}}/dE_\gamma$ are numerically calculated by the complex coordinate rotation method [19, 27–29]. The energy-normalized continuum wave function satisfies

$$|\Psi_{\text{C}}(E_f)\rangle \langle \bar{\Psi}_{\text{C}}(E_f)| = \frac{1}{2i\pi} (G^-(E_f) - G^+(E_f)). \quad (13)$$

The $G^\pm(E_f)$ are the Green functions of the Hamiltonian on the real axis as

$$G^\pm(E_f) = \frac{1}{E_f \pm i\epsilon - H}, \quad (14)$$

where ϵ is a small positive number to avoid singularity. For the complex-rotated Hamiltonian $H(\theta)$, the Eq. (13) can be rewritten as

$$\begin{aligned} & |\Psi_{\text{C}}(E_f)\rangle \langle \bar{\Psi}_{\text{C}}(E_f)| \\ & = \frac{1}{2i\pi} \left[R(-\theta) \frac{1}{H(\theta) - E_f} R(\theta) - R(\theta) \frac{1}{H(-\theta) - E_f} R(-\theta) \right]. \quad (15) \end{aligned}$$

We consider the eigen functions $\{\psi_{J_f,v}(\theta)\}$ where J_f is the total angular momentum quantum number of the whole system of the decay fragments. Under the dipole approximation, $J_f = J \pm 1$. Because the complex-rotated wave functions satisfy the following closure relation,

$$\sum_v |\psi_{J_f,v}(\theta)\rangle \langle \bar{\psi}_{J_f,v}(\theta)| = 1, \quad (16)$$

Eq. (15) becomes

$$|\Psi_C(E_f)\rangle \langle \bar{\Psi}_C(E_f)| = \frac{1}{2i\pi} \left[\frac{R(-\theta) |\psi_{J_f,v}(\theta)\rangle \langle \bar{\psi}_{J_f,v}(\theta)| R(\theta)}{E_{J_f,v}(\theta) - E_f} - \frac{R(\theta) |\psi_{J_f,v}(\theta)\rangle \langle \bar{\psi}_{J_f,v}(\theta)| R(-\theta)}{\bar{E}_{J_f,v}(\theta) - E_f} \right]. \quad (17)$$

We note that the set of eigen functions obtained by the Gaussian expansion method becomes approximately a complete set in a finite region [23]. Using Eq. (17), we have the $d\Gamma_{RC}/dE_\gamma$ in terms of $\{\psi_{J_f,v}(\theta)\}$ as in [19, 29, 30]

$$\frac{d\Gamma_{RC}}{dE_\gamma} = \frac{4}{3} \alpha^3 E_\gamma^3 \frac{1}{\pi} \text{Im} \sum_{v=1}^{v_{\max}} \left[\frac{\langle \bar{\psi}_{J_f,v}(\theta) | \mathbf{d}(\theta) | \Psi_R(\theta) \rangle^2}{E_{J_f,v}(\theta) - E_f} \right], \quad (18)$$

where $\mathbf{d}(\theta)$ is the complex-rotated electric dipole moment operator. The $\Psi_R(\theta)$ is the rotated wave function of the resonance state which is a member of $\{\psi_{J_f,v}(\theta)\}$. For the present system, the wave function of the resonance state Ψ_R has a small scattering component, and the complex-rotated wave function, $\Psi_R(\theta)$, can be expanded in terms of L^2 basis functions with a sufficient accuracy. The number of eigen functions v_{\max} is less than the total number of basis functions N_{\max} , namely $v_{\max} \leq N_{\max}$. We will see in the following section that $d\Gamma_{RC}/dE_\gamma$ converges as increasing v_{\max} . Typically we use $v_{\max} \sim 400$ which is much smaller than $N_{\max} \sim 10^4$.

To estimate the accuracy of our calculations, we calculate $d\Gamma_{RC}/dE_\gamma$ in both length and velocity gauges. Since the accuracy of the long-range component of the wave function affects the length-gauge calculation than velocity-gauge one, the latter is better than the former because the complex coordinate rotation method artificially dampens the outgoing component.

III. RESULTS AND DISCUSSION

A. Energy levels of resonance states

To examine the accuracy of the resonance state wave functions, we investigated the $dd\mu^*$ resonance energies of S , P , D , and F waves using a stabilization method [32–34]. The resonance energy levels of the S and P waves obtained in this study are listed in Table I with the vibrational quantum number v_r and compared with those of several previous studies [18, 19, 31]. Table I expresses the resonance energies by quasi-binding energies,

$$\varepsilon_{J,v_r} = E_{\text{th}}^{(n=2)} - E_{J,v_r}^{(R)}, \quad (19)$$

where $E_{\text{th}}^{(n=2)}$ denotes the $d\mu(n=2) + d$ threshold energy. Our calculations agree well with the latest complex coordinate rotation calculations [19] for $^{1,5}S^e$ and are in reasonable agreement with the stabilization calculations

TABLE I. Comparison of resonance energies calculated in this study with those of previous studies. These values are given in eV relative to the $d\mu(n=2) + d$ threshold energy.

Symmetry	v_r	This work	Ref. [19]	Ref. [18]	Ref. [31]
$^{1,5}S^e$	0	218.111 1	218.111 567	218.112	218.113
$^{1,5}S^e$	1	135.278 5	135.279 003	135.279	135.278
$^{1,5}S^e$	2	72.966 2	72.967 058	72.697	72.962
$^{1,5}S^e$	3	31.901 1	31.901 769	31.902	31.884
$^{1,5}S^e$	4	12.616 5	12.616 688	12.617	12.606
$^{1,5}S^e$	5	5.311 2	5.311 346	5.311	5.304
$^{1,5}S^e$	6	2.275 0	2.275 273		2.210
$^{1,5}S^e$	7	0.981 0	0.981 232		
$^{1,5}S^e$	8	0.424 1			
$^3S^e$	0	21.1551			21.156
$^3S^e$	1	9.4149			9.415
$^3S^e$	2	4.0801			4.080
$^3S^e$	3	1.7656			1.603
$^3S^e$	4	0.7645			
$^3S^e$	5	0.3311			
$^3P^o$	0	211.9236			211.926
$^3P^o$	1	130.3486			130.348
$^3P^o$	2	69.2351			69.225
$^3P^o$	3	29.5255			29.504
$^3P^o$	4	11.4945			11.478
$^3P^o$	5	4.7732			4.758
$^3P^o$	6	2.0157			1.913
$^3P^o$	7	0.8567			
$^3P^o$	8	0.3650			
$^{1,5}P^o$	0*	22.6458			22.648
$^{1,5}P^o$	0	20.1211			20.122
$^{1,5}P^o$	1	8.8046			8.805
$^{1,5}P^o$	2	3.7575			3.749
$^{1,5}P^o$	3	1.6023			1.395
$^{1,5}P^o$	4	0.6837			
$^{1,5}P^o$	5	0.2918			

[31] for $^3S^e$, $^3P^o$, and $^{1,5}P^o$. The resonance widths of the non-radiative decay are too small to be determined using the present complex coordinate rotation calculation and are estimated to be less than $\lesssim 10^{-7}$ hartree. The non-radiative decay rate is about 0.01 ps^{-1} which is more than two orders of magnitude slower than the radiative decay rate.

By applying the Born-Oppenheimer approximation to the $d+d+\mu$ system, three adiabatic potential energy curves, $3d\sigma_g$, $4f\sigma_u$, and $2p\pi_u$, are obtained. They are attractive at long inter-nuclear distances and approach asymptotically to the $d\mu(n=2) + d$ threshold energy. Both $3d\sigma_g$ and $4f\sigma_u$ potential energy curves are inversely proportional to the square of the distance at long distances. In contrast, the $2p\pi_u$ potential is inversely proportional to the fourth power of the distance. Figure 2 illustrates these adiabatic potential energy curves as well as $1s\sigma_g$ and $2p\sigma_u$ curves. The resonance states of $^{1,5}S^e$ and $^3P^o$ are considered to belong to the $3d\sigma_g$ adiabatic potential energy curve, and the other resonance states of $^3S^e$ and $^{1,5}P^o$, except for the $v_r = 0^*$ state of $^{1,5}P^o$, be-

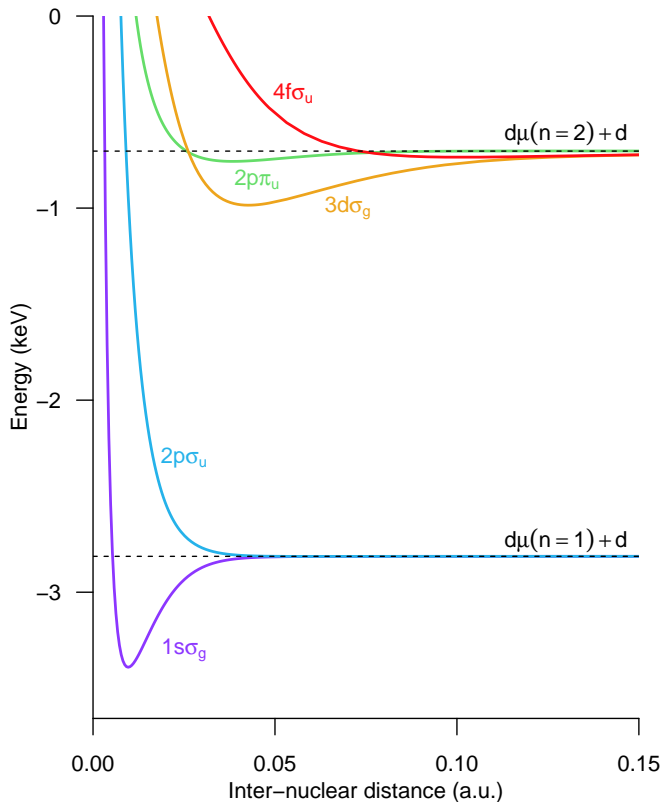


FIG. 2. Adiabatic potential energy curves for $dd\mu$. The lower and upper dashed lines correspond to $d\mu(n=1)+d$ and $d\mu(n=2)+d$, respectively.

long to the $4f\sigma_u$ adiabatic potential energy curve. The $v_r = 0^*$ state of $^{1,5}P^o$ is referred to as an even-parity bound state [31] and is supported by the $2p\pi_u$ potential.

The degeneracy of $d\mu(2s)$ and $d\mu(2p)$ causes Stark mixing owing to the charge of the other d , resulting in an infinite series of the resonance energy levels, which is called the dipole series. The resonance states of the dipole series are supported by an attractive ion-dipole interaction, which is proportional to the inverse of the square of the $d\mu$ - d distance. However, as the degeneracy of $n=2$ levels of $d\mu$ is resolved mainly by vacuum polarization, the resonance series is truncated at high vibration levels. As vacuum polarization results in an approximately 0.2 eV $2s$ - $2p$ interval, we enlarged the expansion range of the basis functions to ~ 240 m.a.u. such that a shallow resonance state can be described with good accuracy.

The energy intervals of the dipole resonance states near the threshold energy obey the following simple analytical formula.

$$\frac{\varepsilon_{J,v_r}}{\varepsilon_{J,v_r+1}} = \exp\left(\frac{2\pi}{\alpha_J}\right), \quad (20)$$

where α_J is a constant that depends on the total angular

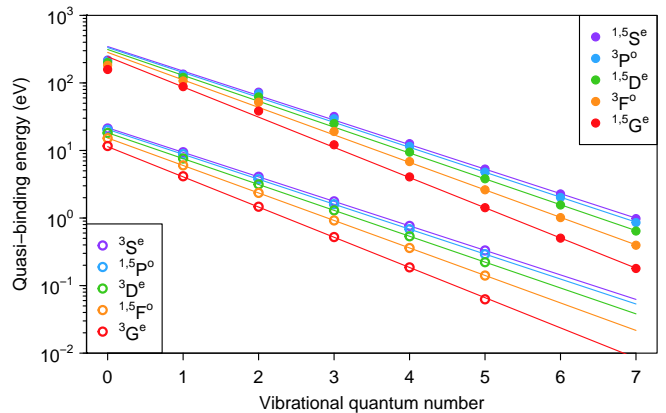


FIG. 3. Quasi binding energies of $dd\mu^*$ resonance states are presented against the corresponding vibrational quantum numbers. The lines are fitted using an exponential function.

momentum J and reduced masses as

$$\alpha_J = \sqrt{-\frac{1}{4} - J^2 + J + 1 + (2J + 1)\gamma_J}. \quad (21)$$

Here,

$$\gamma_J = \sqrt{\left(\frac{6\mu_{d,\mu}}{\mu_{d,\mu}(2J+1)}\right)^2 + 1}, \quad (22)$$

where $\mu_{d,\mu}$ and $\mu_{d,\mu,d}$ are reduced masses of $d + \mu$ and $d\mu + d$, respectively. The values of α_J for the $dd\mu^*$ resonances are $\alpha_{J=0} = 1.197$, $\alpha_{J=1} = 1.176$, $\alpha_{J=2} = 1.134$, $\alpha_{J=3} = 1.067$, and $\alpha_{J=4} = 0.971$.

Figure 3 presents the quasi-binding energies ε_{J,v_r} versus v_r . The dashed lines are fitted by

$$\varepsilon_{J,v_r} = A \exp\left(-\frac{2\pi}{\alpha_J} v_r\right). \quad (23)$$

Using the analytical values of α_J in Eq. (21), we optimized A for the high vibrational states as follows: $4 \leq v_r \leq 7$ for $^{1,5}S^e$, $^3P^o$, $^{1,5}D^e$, $^3F^o$, and $^{1,5}G^e$ resonances and $3 \leq v_r \leq 5$ for $^3S^e$, $^{1,5}P^o$, $^3D^e$, $^{1,5}F^o$, and $^3G^e$ resonances. It can be observed that the energy interval of these high vibrational states demonstrates good agreement with the analytical expression, that is, the obtained $dd\mu^*$ resonance energies are considered to be accurate.

B. Convergence of x-ray spectrum

We examine the convergence of the x-ray spectra from the decay of the resonance states into a continuum using Eq. (18). Figure 4 presents the convergence of the x-ray spectrum from the $^{1,5}S^e, v_r = 0$ state against the complex coordinate rotation angle θ . At $\theta = 0.10$, the spectrum

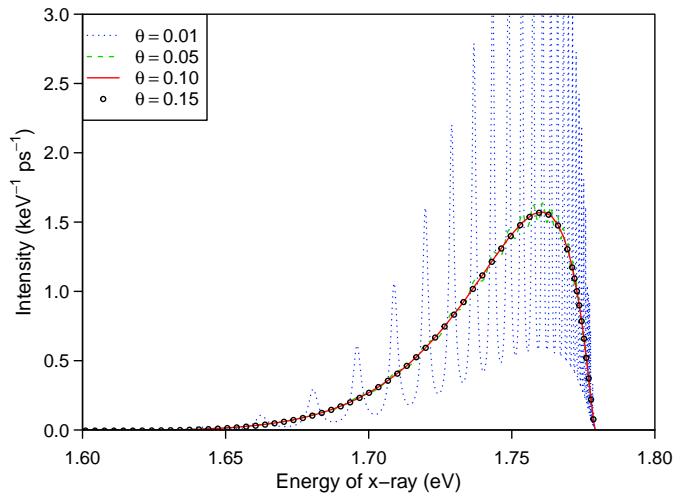


FIG. 4. Convergence of x-ray spectrum for the $^{1,5}S^e v_r = 0$ state against the complex coordinate rotation angle θ .

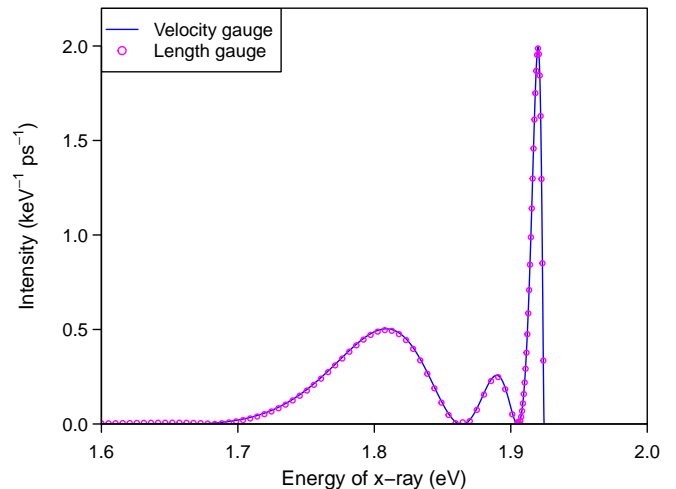


FIG. 6. Comparison of the velocity and length gauge calculations for the $^{1,5}S^e v_r = 2$ state.

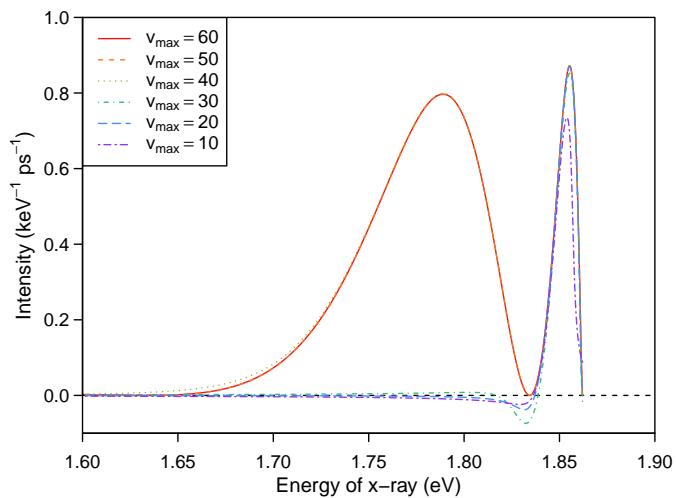


FIG. 5. Convergence of x-ray spectrum for $^{1,5}S^e v_r = 1$ state against the maximum number of eigen functions v_{\max} .

exhibits an oscillation against the x-ray energy, while the oscillation disappears as θ increases. The antinodes of the oscillation appear when the denominator $(E_{J,v}(\theta) - E_f)$ in Eq. (18) is approximately zero at small θ while the $E_{J,v}(\theta)$ is a complex value with a non-zero imaginary part such that $(E_{J,v}(\theta) - E_f)^{-1}$ is non-singular at all E_f values in the continuum state. In the present calculation, we confirmed that $\theta \geq 0.1$ results in a well-converged x-ray spectrum.

In terms of the accuracy of the wave functions of the resonance states, we use sufficient number of basis functions and examine the Gaussian size parameters in Eq. (10) such that the well converged energies are ob-

tained for low v_r states and physically meaningful dipole series are reproduced for high v_r states.

To examine the validity of the approximation for the calculation of the x-ray spectra described by Eq. (18), we examine the convergence of the x-ray spectra by increasing the number of eigen functions $\{\psi_{J,v}(\theta)\}$, v_{\max} , used in Eq. (18). We sorted $\{\psi_{J,v}(\theta)\}$ in ascending order of $\text{Re} E_{J,v}(\theta)$ and increased v_{\max} . Figure 5 presents an example of the convergence behavior against v_{\max} for the $^{1,5}S^e v_r = 1$ state. In this calculation, $\theta = 0.15$ is used. We conclude that spectra are converged against the $v_{\max} \geq 50$. A drastic change occurs between $v_{\max} = 30$ and 40 where a lower peak is observed. $\text{Re} E_{J,v=30} = -0.473323$ m.a.u. and $\text{Re} E_{J,v=40} = -0.445569$ m.a.u., which correspond to the x-ray energies E_γ of 1.86 keV and 1.71 keV, respectively. Calculations for $v_{\max} \leq 30$ do not describe the continuum states corresponding to E_γ at approximately 1.7 keV, but by using $v_{\max} \geq 40$, the energy of the continuum states that can be described by the superposition of complex rotated wave functions increases, and the x-ray spectrum can be obtained accurately over a wide energy range.

We also examine the x-ray spectrum by comparing the length- and velocity-gauge calculations. Figure 6 presents an example of the length- and velocity-gauge calculations for the $^{1,5}S^e v_r = 2$ state using the same basis functions and complex rotation angle. The x-ray spectra obtained using two kinds of gauges exhibit excellent agreement with each other, which confirms the validity of our calculations.

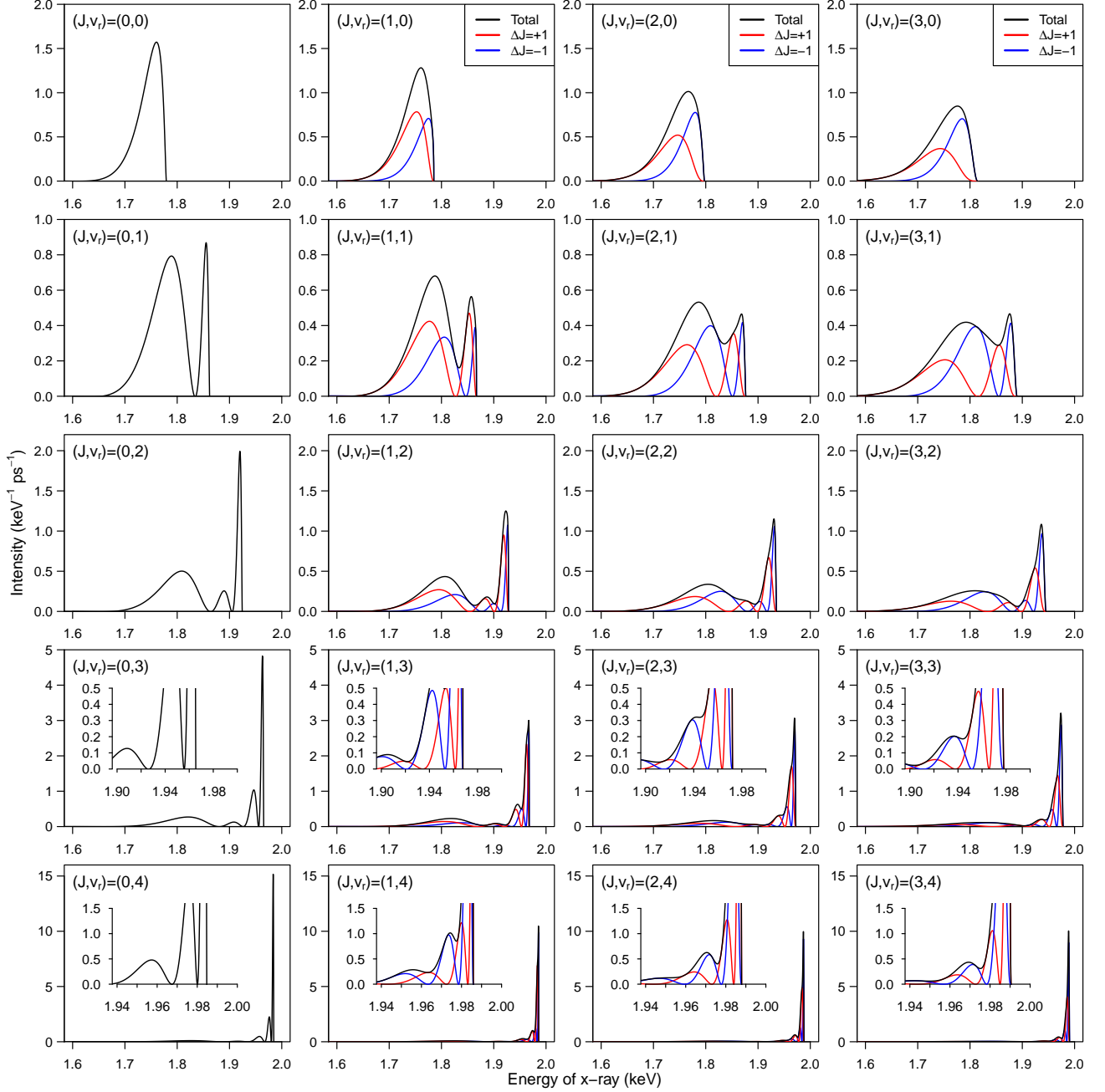


FIG. 7. X-ray spectra of radiative decay into continuum from resonance states belonging to $^{1,5}S^e$, $^3P^o$, $^{1,5}D^e$, and $^3F^o$ series.

C. Characteristic shape of x-ray spectrum

Figures 7, 8, 9, and 11 present a summary of the x-ray spectra of radiative decay in the continuum state for each resonance state. The maximum x-ray energy corresponds to the energy interval between the resonance energy $E_{J,v_r}^{(R)}$ and $d\mu(n=1) + d$ dissociation threshold energy $E_{th}^{(n=1)}$

as follows:

$$E_\gamma \leq E_{J,v_r}^{(R)} - E_{th}^{(n=1)}. \quad (24)$$

For the $J = 0$ resonance states, radiative decay results in a $J = 1$ continuum state, within the dipole approximation. As we do not include spin-dependent interactions between the two deuterons in the present calculation, the total nuclear spin angular momentum conserves throughout the radiative decay. For $J \geq 1$ resonance

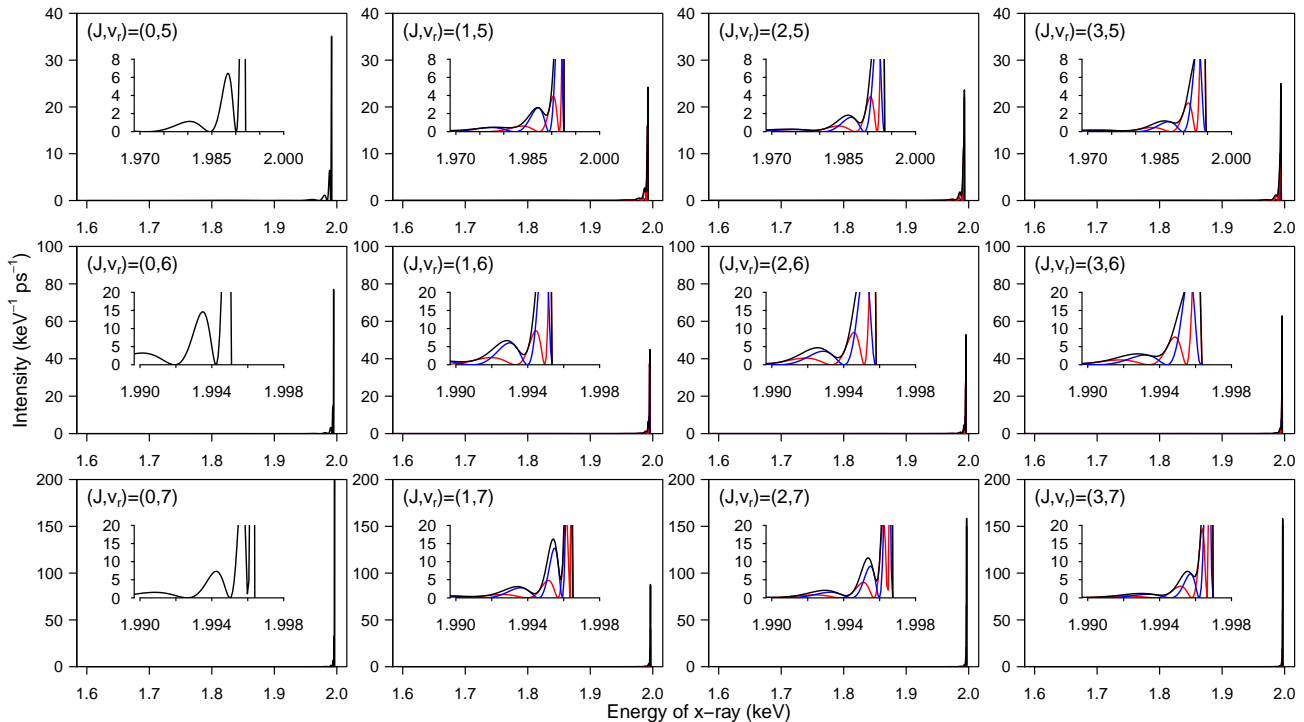


FIG. 8. (Continued from Fig. 7.)

states, the radiative decay results in $J \pm 1$ continuum states. We distinguish between the J -increasing decay and J -decreasing decay by denoting $\Delta J = \pm 1$.

As shown in Fig. 7, which summarizes the spectra of the resonance states belonging to $3d\sigma_g$ series, the x-ray spectrum from $1,^5S^e$ resonance states increases the number of nodes with an increase in v_r . A similar trend can be observed for higher angular momenta, whereas the node structure is evident only for the partial spectra and disappears from the total x-ray spectrum because of the shift in the node positions. The decrease of x-ray spectra of $\Delta J = +1$ decay near the maximum x-ray energy is steeper than those of $\Delta J = -1$ because of centrifugal repulsion between the decay fragments.

Figure 8 summarizes the x-ray spectra of the $v_r \geq 5$ resonance states of the $3d\sigma_g$ series. The number of the nodes in the x-ray spectrum increases as an increase of v_r . The intensity near the maximum x-ray energy increases as an increase of v_r . For the resonance states of the $4f\sigma_u$ series, as shown in Fig. 9, a similar trend can be observed, i.e., the number of nodes increases with v_r . It should be noted that the $4f\sigma_u$ resonances have a shallower quasi-binding energy than the $3d\sigma_g$ resonances with the same v_r .

To investigate characteristic shape of the x-ray spectrum, we consider the vertical transition between the resonance and continuum states. Radial distribution func-

tions of the resonance states are calculated by

$$D(R'_1) = R_1'^2 \left\langle \Psi_R \left| \frac{\delta(R_1 - R'_1)}{4\pi R_1^2} \right| \Psi_R \right\rangle, \quad (25)$$

where R_1 denotes the distance between the center-of-mass of d_p and d . Here, we use the unrotated wave function Ψ_R . This approximation is appropriate when the energy widths of the resonance states are much smaller than the resonance energy. In the present case, the resonance width against the non-radiative decay is sufficiently small (less than 10 μeV [19]), and then we can treat $\Psi_R(\theta = 0)$ as a resonance-state wave functions in Eq. (25) to discuss the origin of the characteristic shapes of the x-ray spectra.

Figure 10 presents the radial distribution functions of the resonance states. As expected, the radial distribution functions increase their number of nodes as the vibrational quantum number v_r increases. The resonance states in the $3d\sigma_g$ series ($1,^5S^e$, $3P^o$, $1,^5D^e$, $3F^o$, and $1,^5G^e$) exhibit a relatively compact distribution in comparison with those in the $4f\sigma_u$ series ($3S^e$, $1,^5P^o$, $3D^e$, $1,^5F^o$, and $3G^e$). This is consistent with the adiabatic potential energy curves presented in Fig. 2, i.e., the $4f\sigma_u$ adiabatic potential energy curve is more repulsive at short distances and has a shallower well compared to the $3d\sigma_g$ adiabatic potential energy curve. The resonance states denoted by $v_r = 0^*$ in $1,^5P^o$ and $3D^e$ have significantly compact distributions. These resonance states

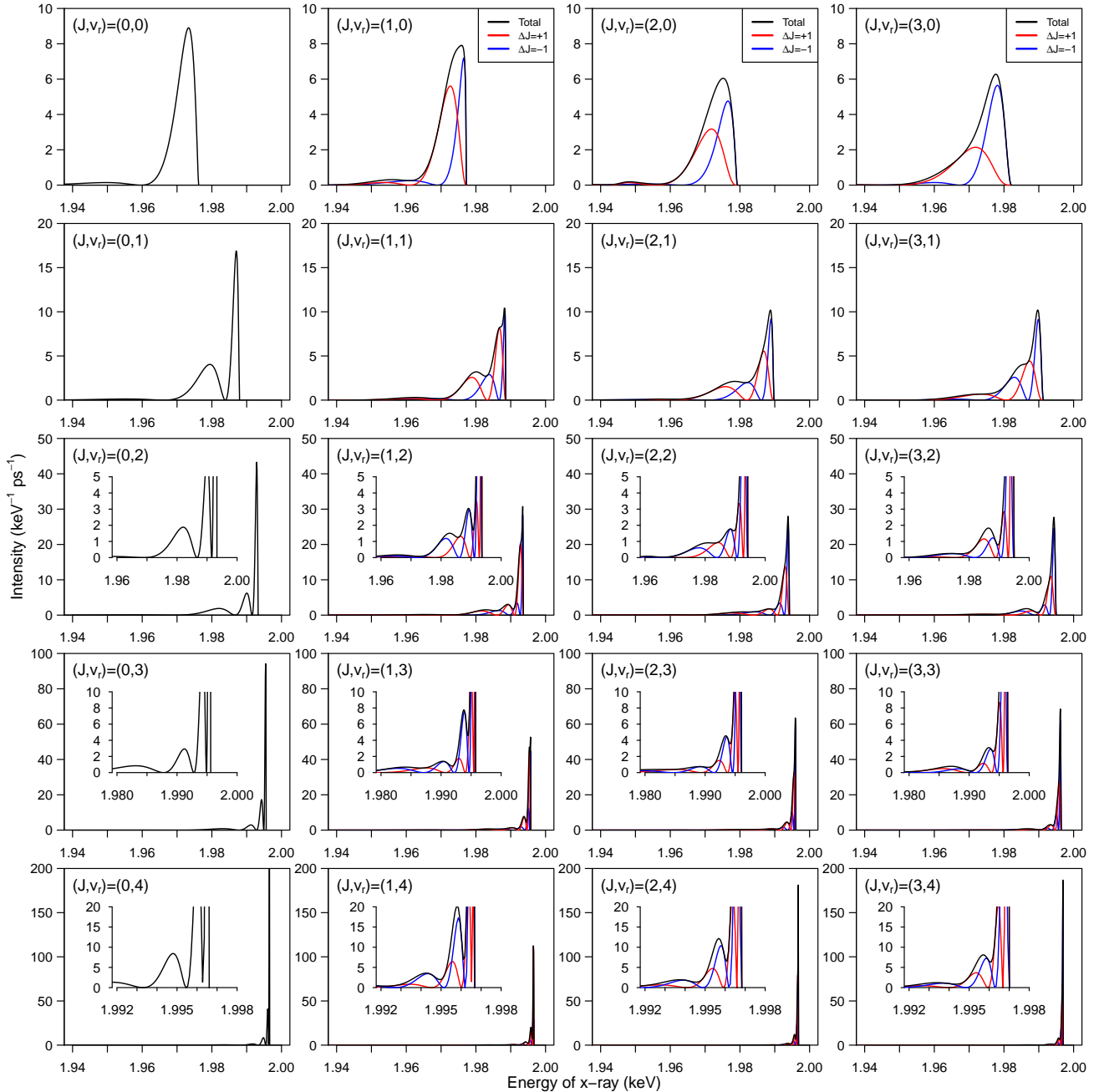


FIG. 9. X-ray spectra of radiative decay into continuum from resonance states belonging to ${}^3S^o$, ${}^{1,5}P^e$, ${}^3D^o$, and ${}^{1,5}F^e$ series.

belong to the $2p\pi_u$ series, and their compact distribution is consistent with the short-range adiabatic potential energy curve of $2p\pi_u$.

As indicated in Ref. [18], an x-ray spectrum can be qualitatively understood as a vertical transition from the resonance energy level to the dissociative $2p\sigma_u$ potential energy curve. Thus, the minimum x-ray energy is limited by the repulsive $2p\sigma_u$ potential energy curve $V_{2p\sigma_u}(R_1)$

as follows:

$$E_\gamma \geq E_{J,v_r}^{(R)} - V_{2p\sigma_u}(R_1^{\text{IT}}), \quad (26)$$

where R_1^{IT} denotes the inner turning distance of the resonance state. As the adiabatic potential $V_{2p\sigma_u}(R_1)$ is strongly repulsive at short distances and asymptotically converges to the threshold energy of $d\mu(1s) + d$, the compact structure of the resonance state tends to result in a widely distributed x-ray spectrum, and the diffused

structure tends to produce a sharp x-ray spectrum near the maximum x-ray energy, which is consistent with the calculated spectra presented in Figs. 7, 8, and 9.

Figure 11 presents the x-ray spectra of the two states of $v_r = 0^*$ supported by the $2p\pi_u$ adiabatic potential energy curve. As listed in Table I, the quasi-binding energy of $v_r = 0^*$ in $^{1,5}P^o$ is 22.6 eV, which differs only by 2.5 eV from the $v_r = 0$ state in $^{1,5}P^o$ ($4f\sigma_u$ series). However, on comparing the x-ray spectrum of Fig. 11 (J, v_r) = (1, 0) with Fig. 9 (J, v_r) = (1, 0), it is observed that the x-ray spectrum from $v_r = 0^*$ in the $2p\pi_u$ series is broader than the $v_r = 0$ state in the $4f\sigma_u$ series. A similar trend is observed for the $v_r = 0^*$ state in $^3D^e$.

D. Kinetic energy distribution of the decay fragments

The total released energy $E_{J, v_r}^{(R)} - E_{\text{th}}^{(n=1)}$ by the radiative decay is a sum of the x-ray energy (E_γ) and kinetic energy (K) of the relative motion between $\text{d}\mu(1s)$ and d as

$$E_{J, v_r}^{(R)} - E_{\text{th}}^{(n=1)} = E_\gamma + K. \quad (27)$$

As observed in Figs. 7, 8, and 9, each partial x-ray spectrum corresponding to the $\Delta J = \pm 1$ decay has clear nodes. This implies that the kinetic energy distribution of the relative motion of the decay fragments also contains nodes depending on the angular momentum of their relative motion L_f . Denoting the kinetic energy distribution by $f(K)$, the kinetic energy nodes K_{node} are defined to satisfy

$$\left. \frac{df(K)}{dK} \right|_{K=K_{\text{node}}} = 0, \quad \left. \frac{d^2f(K)}{dK^2} \right|_{K=K_{\text{node}}} > 0. \quad (28)$$

Similarly, radial distribution functions also have nodes at certain distances $R_1 = R_{\text{node}}$. Assuming vertical transitions from the resonance state to a lower dissociative potential energy curve, the kinetic energy node K_{node} can be associated with the distance node R_{node} of the radial distribution function, as illustrated in Fig. 12.

We analyze the relationship between K_{node} and R_{node} as shown in Fig. 13 by specifying L_f . It is apparent that, at the same R_{node} , K_{node} is higher at a higher L_f . To quantitatively investigate the $K_{\text{node}}-R_{\text{node}}$ relationship, we introduce an adiabatic estimation of K_{node} using

$$K_{\text{node}}^{(\text{ad})}(R_{\text{node}}) = V_{2p\sigma_u}(R_{\text{node}}) + \frac{L_f(L_f + 1)}{2\mu_{\text{d}\mu, \text{d}}R_{\text{node}}^2}, \quad (29)$$

where $V_{2p\sigma_u}$ is the $2p\sigma_u$ adiabatic potential energy curve measured from the threshold energy of $\text{d}\mu(1s)+\text{d}$, and $\mu_{\text{d}\mu, \text{d}}$ is the reduced mass of $\text{d}\mu$ and d . Equation (29) indicates that a higher L_f results in a higher centrifugal barrier between the decay fragments and a higher K_{node} at the same distance node, which is qualitatively consistent with the trend presented in Fig. 13.

The estimated $K_{\text{node}}^{(\text{ad})}$ values are presented in Fig. 13 by solid lines. In the case $L_f = 0$, the estimated $K_{\text{node}}^{(\text{ad})}(R_{\text{node}})$ fails to explain the K_{node} derived from the three-body calculation. In particular, $V_{2p\sigma_u}$ has a shallow attractive well at a large distance; therefore, $K_{\text{node}}^{(\text{ad})}(R_{\text{node}})$ becomes negative at large distances. In the non-zero L_f case, the decreasing behavior of K_{node} against R_{node} demonstrates a trend similar to the $E_{\text{node}}^{(\text{ad})}(R_{\text{node}})$; however, even at $L_f = 4$, $K_{\text{node}}^{(\text{ad})}(R_{\text{node}})$ does not coincide with the K_{node} .

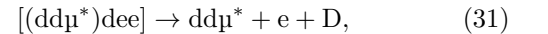
We can assume a simpler model of the kinetic energy node as

$$K_{\text{node}}^{(\text{st})}(R_{\text{node}}) = \frac{\exp(-2R_{\text{node}}/a_\mu)}{R_{\text{node}}} + \frac{L_f(L_f + 1)}{2MR_{\text{node}}^2}, \quad (30)$$

where the first term denotes the screened Coulomb potential between $\text{d}\mu(1s)$ and d . a_μ denotes a Bohr radius of $\text{d}\mu(1s)$. In contrast with $V_{2p\sigma_u}(R_{\text{node}})$, the screened Coulomb potential is repulsive to any R_{node} ; however, $K_{\text{node}}^{(\text{st})}(R_{\text{node}})$ fails to reproduce K_{node} in the three-body calculation, as indicated by the dashed lines in Fig. 13. The discrepancy between the K_{node} and $K_{\text{node}}^{(\text{ad/st})}$ reaches nearly 100 eV.

Therefore, the radiative decay into the continuum does not occur *on to* the dissociative potential energy curve depicted in the adiabatic model. The decay fragments have much higher kinetic energies than the adiabatic potential curve provides. Non-adiabatic calculations are indispensable for determining the kinetic energy distribution and x-ray spectra.

The kinetic energy distribution of decay fragments is an interesting subject in the context of the muon catalyzed fusion. Figure 14 presents a summary of the kinetic energy distribution from $0 \leq v_r \leq 3$ resonance states of the $3d\sigma_g$ series. When the $\text{dd}\mu^*$ resonance state forms via the Vesman mechanism as shown in Eq. (1), $\text{dd}\mu^*$ is in the electron cloud of the host molecule [$(\text{dd}\mu^*)\text{dee}$]. The rates of the Auger transition,



are much higher than the radiative decay rates, the $\text{dd}\mu^*$ first emits an Auger electron and is deexcited to lower rovibrational states (Auger decay). Because the Auger decay requires energy interval of 15.4 eV to overcome the ionization energy of hydrogen molecule, the radiative decay dominates for $0 \leq v_r \leq 3$ resonance states of the $3d\sigma_g$ series. After the radiative decay, a part of the released energy $E_{J, v_r}^{(R)} - E_{\text{th}}^{(n=1)}$ is kinetic energy of the decay fragments which can induce the epithermal process in μCF . A more detailed investigation of the Auger processes will be presented in our future publication.

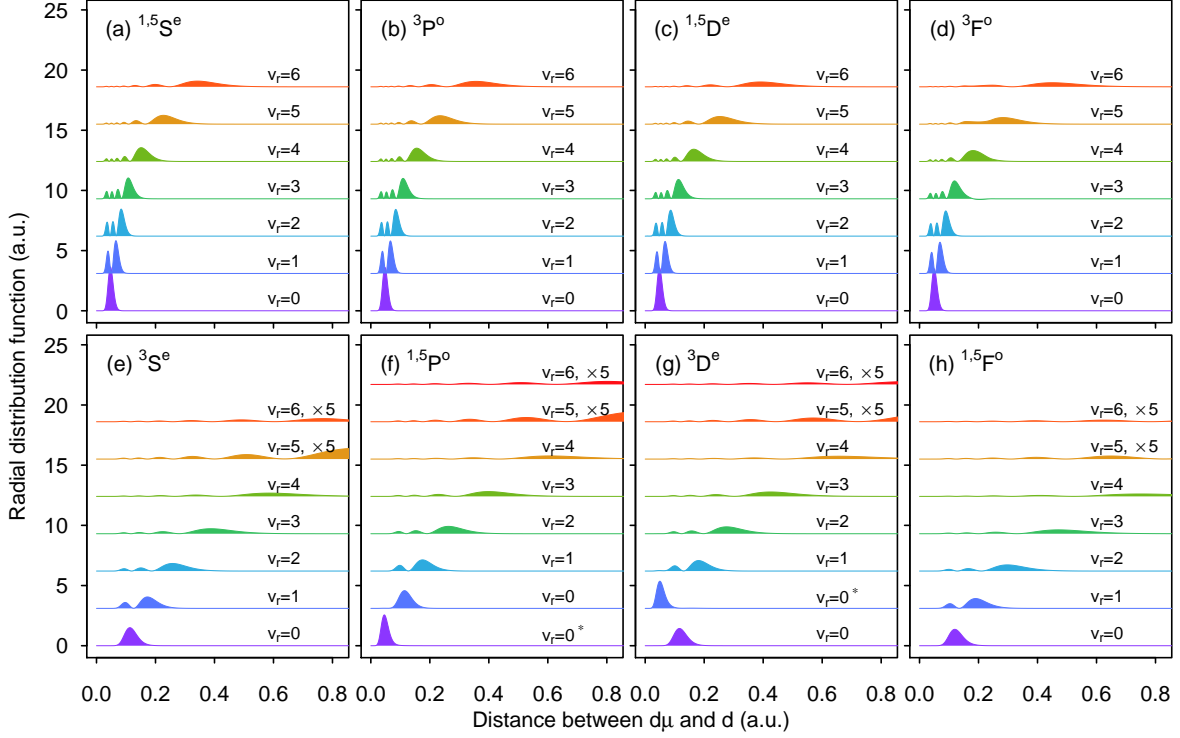


FIG. 10. Radial distribution functions of $dd\mu^*$ are presented as a function of the distance between the center-of-mass of $d\mu$ and d .

E. Contribution from radiative decay into bound state

The total rates of radiative decay into the continuum state can be obtained by integrating the x-ray spectrum $d\Gamma_\gamma/dE_\gamma$ over E_γ . In addition to the decay into the continuum state, we investigate the radiative decay into the bound states (RB decay),

$$dd\mu^*(J, v_r) \rightarrow dd\mu(J_f, v_b) + \gamma, \quad (32)$$

and into the other resonance states (RR' decay),

$$dd\mu^*(J, v_r) \rightarrow dd\mu^*(J_f, v_r') + \gamma. \quad (33)$$

These rates can be calculated as

$$\Gamma_{RB(RR')} = \frac{4}{3} \alpha^3 E_\gamma^3 \text{Re} \langle \bar{\Psi}_{B(R')}(\theta) | \mathbf{d}(\theta) | \Psi_R(\theta) \rangle^2, \quad (34)$$

where $\Psi_R(\theta)$ is a complex rotated wave function of the resonance states, $\Psi_B(\theta)$ is that of the final bound state, and $\Psi_{R'}(\theta)$ is that of the other resonance state. E_γ corresponds to the energy interval between the initial and final state energies.

Table II lists $\Gamma_{RB(RR')}$ in the descending order. These rates agree well with each other in both the length and velocity gauges. The largest rates are found for RB decay from the $v_r = 0^*$ state in ${}^3D^e$ and ${}^{1.5}P^o$. These

resonance states are supported by the $2p\pi_u$ adiabatic potential curve and their radial distribution function has a peak at relatively short distance, namely at 0.045 bohr for $v_r = 0^*$ state of ${}^{1.5}P^o$ and 0.050 bohr for that of ${}^3D^e$, as shown in Fig. 10(f) and (g). The $v_r = 0$ states in ${}^3S^e$ and ${}^3D^e$ also exhibit relatively larger rates than the others while the radial distribution functions of these resonance states have peaks longer than 0.11 bohr. Both the states result in the bound state $(J, v_b) = (1, 1)$, which is a loosely bound state having a binding energy of only 1.97 eV and a diffused radial distribution function. Thus, the compact wave functions in resonance states or diffused wave functions in the final states lead to exhibit relatively high RB decay rates.

Table III summarizes the radiative decay rates along with the RB+RR' decay rates for each resonance state. The total decay rates into a continuum, denoted by Γ_{RC} , are obtained by numerical integration of the x-ray spectrum, as shown in Eq. (11). Γ_{RC} is the sum of $\Gamma_{RC(-)}$ and $\Gamma_{RC(+)}$, which are the J -decreasing and J -increasing decay rates, respectively. The radiative decay rates listed in this table are obtained using a velocity gauge, and the significant digits are estimated from the comparison with the length-gauge calculations. For some high vibrational states, the radiative decay rates into the continuum could not be determined using length-gauge calculations. As the bound states exist only in ${}^{1.5}S^e$, ${}^3P^o$, and ${}^{1.5}D^e$

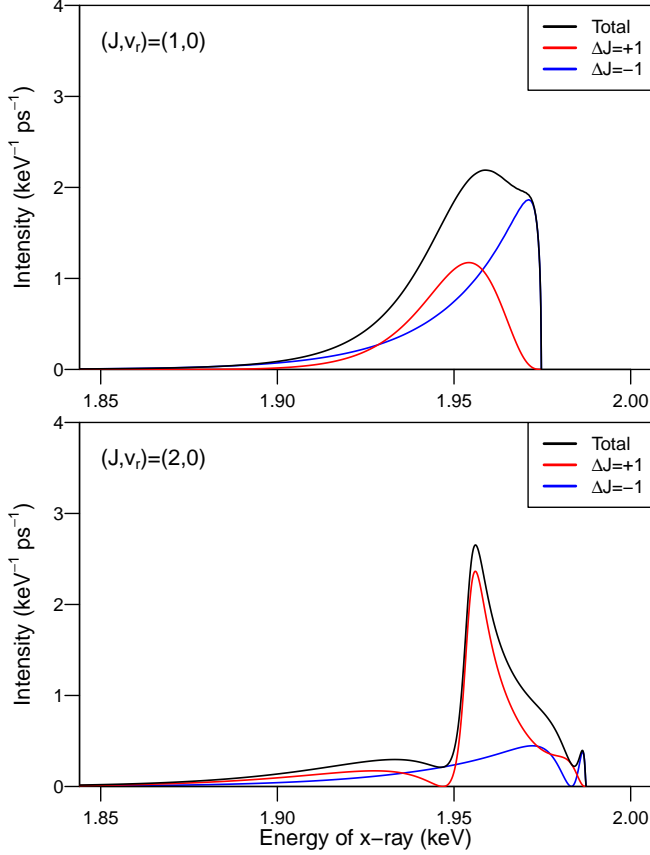


FIG. 11. X-ray spectra from $v_r = 0^*$ states in $1,5P^o$ (upper panel) and $v_r = 0^*$ (lower panel).

symmetries, the resonance states $v_r \leq 3$ in $1,5S^e$, $3P^o$, $1,5D^e$, and $3F^o$ symmetries exhibited neither resonance-to-resonance nor resonance-to-bound decay branches under dipole approximation. Γ_{RC} can be compared with a $d\mu(2p) \rightarrow d\mu(1s)$ transition rate of 0.12270 ps^{-1} . As shown in Fig. 3, the $dd\mu^*$ resonance states at high vibrational states can be considered as members of the dipole series in which the wave function involves a mixed fraction of $d\mu(2s)$ and $d\mu(2p)$. The radiative decay rates at the high vibrational states are similar to half the value of the $d\mu(2p) \rightarrow d\mu(1s)$ transition rate, 0.06135 ps^{-1} .

F. Branching ratios into bound state from $dd\mu^*$ and $dt\mu^*$

It is unexpected that the radiative decay rates into the bound and resonance states ($\Gamma_{RB+RR'}$) of $v_r = 0^*$ states in $3D^e$ and $1,5P^o$ are comparable with the radiative decay rates into the continuum. The branching ratio of the decay rate into the bound state (Γ_{RB}) against the total

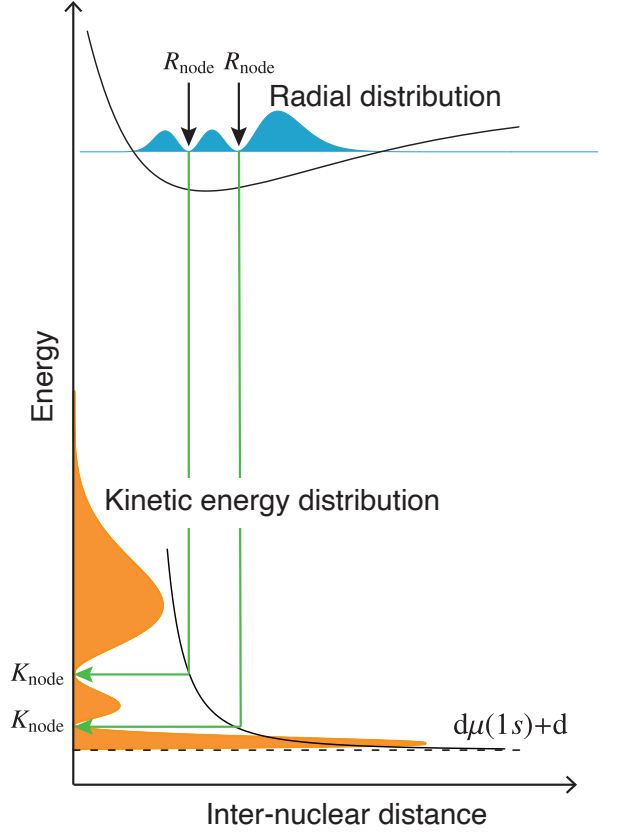


FIG. 12. Schematic of the relationship between the node of the kinetic energy distribution K_{node} and the node of radial distribution R_{node} of the resonance states. Assuming vertical transitions onto the repulsive potential energy curve of the decay fragments, the shorter R_{node} can correspond to a higher K_{node} .

radiative decay rate ($\Gamma_{RC} + \Gamma_{RB}$)

$$\Upsilon_{RB} = \frac{\Gamma_{RB}}{\Gamma_{RC} + \Gamma_{RB}}, \quad (35)$$

is an intriguing quantity for applications of μCF . The radiative decay into the bound state should be a fast track in the μCF cycle because it skips the slow process of the bound state formation and accelerate the μCF cycles. Moreover, the decay into the continuum could prevent the muonic molecule formation and decelerate μCF cycles. Therefore, we have calculated the radiative decay rates of $dt\mu^*$ in addition to the $dd\mu^*$ and examined the branching ratio Υ_{RB} in Table IV.

In contrast to $dd\mu^*$, $dt\mu^*$ is a hetero-nuclear system, and the resonance series are separated only by the total angular momentum J . The vibrational quantum number v_r of $dt\mu^*$ is determined from the lowest resonance state $v_r = 0$ although each resonance state has a major association with one of the three adiabatic series $2p\pi_u$, $3d\sigma_g$, and $4f\sigma_u$ and with one of the dissociation thresholds

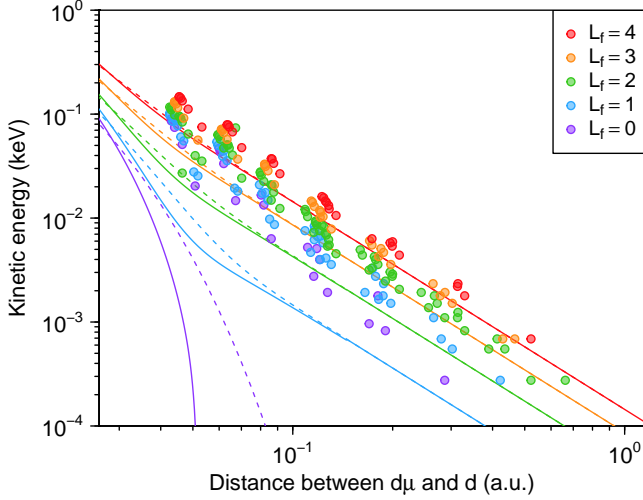


FIG. 13. Nodes of kinetic energy distribution K_{node} of relative motion of the decay fragments are plotted by points against the node of radial distribution R_{node} of the resonance states. The solid lines are given by $K_{\text{node}}^{(\text{ad})}(R_{\text{node}})$, and the dashed line is given by $K_{\text{node}}^{(\text{st})}(R_{\text{node}})$.

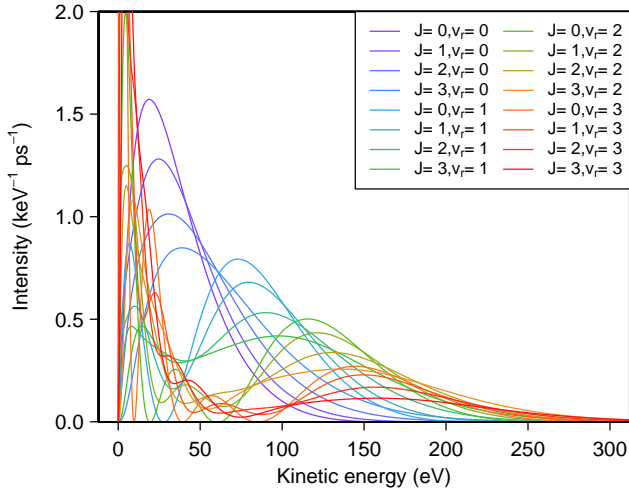


FIG. 14. Kinetic energy distribution of the decay fragments in the center-of-mass framework for $0 \leq v_r \leq 3$ resonance states of the $3d\sigma_g$ series.

$t\mu(n=2)+d$ and $d\mu(n=2)+t$. As expected, a significantly high branching ratio Υ_{RB} are obtained for the D state ($J=2, v_r=7$) and P state ($J=1, v_r=4$). These resonance states are similar to the $v_r=0^*$ resonance states of ${}^3D^e$ and ${}^{1,5}P^o$ in $dd\mu^*$ and can be categorized into the $2p\pi_u$ series. The $J=2, v_r=7$ state results in $J_f=1, v_b=1$ -bound state, which has a binding energy of only 0.66 eV, while the $J=1, v_r=4$ state results in $J_f=0, v_b=1$, which has a binding energy of 34.8 eV.

TABLE II. Resonance-to-bound state transition rates are displayed along with the corresponding x-ray energies. v_r denotes the vibrational quantum number of resonance states, and v_b denotes that of bound states. The rates are listed in descending order of the resonance-to-bound state transition rates. The notation $x[y]$ represents $x \times 10^y$.

Initial state	Final state	E_γ (eV)	$\Gamma_{\text{RB(RR)}}$ (ps^{-1})
${}^3D^e$ $v_r=0^*$	${}^3P^o$ $v_b=1$	1989.35	5.624[-2]
${}^{1,5}P^o$ $v_r=0^*$	${}^{1,5}S^e$ $v_b=1$	2010.56	3.513[-2]
${}^3S^e$ $v_r=0$	${}^3P^o$ $v_b=1$	1978.18	5.658[-3]
${}^3D^e$ $v_r=0$	${}^3P^o$ $v_b=1$	1981.19	3.442[-3]
${}^{1,5}P^o$ $v_r=0^*$	${}^{1,5}D^e$ $v_b=0$	2061.21	3.301[-3]
${}^{1,5}P^o$ $v_r=0^*$	${}^{1,5}S^e$ $v_b=0$	2299.78	9.314[-4]
${}^3D^e$ $v_r=0^*$	${}^3P^o$ $v_b=0$	2214.05	7.683[-4]
${}^{1,5}P^o$ $v_r=0^*$	${}^{1,5}S^e$ $v_r=0$	195.46	4.440[-4]
${}^3S^e$ $v_r=2$	${}^3P^o$ $v_b=1$	1995.26	4.411[-4]
${}^3D^e$ $v_r=0^*$	${}^3P^o$ $v_r=0$	201.93	3.711[-4]
${}^3S^e$ $v_r=1$	${}^3P^o$ $v_b=1$	1989.92	3.660[-4]
${}^3D^e$ $v_r=0^*$	${}^3F^o$ $v_r=0$	172.47	2.710[-4]
${}^3D^e$ $v_r=1$	${}^3P^o$ $v_b=1$	1991.73	2.667[-4]
${}^{1,5}P^o$ $v_r=0^*$	${}^{1,5}D^e$ $v_r=0$	177.20	2.269[-4]
${}^3S^e$ $v_r=3$	${}^3P^o$ $v_b=1$	1997.57	1.565[-4]
${}^{1,5}P^o$ $v_r=0$	${}^{1,5}S^e$ $v_b=1$	2013.09	9.255[-5]
${}^3S^e$ $v_r=4$	${}^3P^o$ $v_b=1$	1998.57	6.767[-5]
${}^3S^e$ $v_r=0$	${}^3P^o$ $v_r=1$	109.19	3.514[-5]
${}^3S^e$ $v_r=0$	${}^3P^o$ $v_r=2$	48.07	3.215[-5]
${}^3S^e$ $v_r=1$	${}^3P^o$ $v_r=1$	120.93	3.022[-5]
${}^3S^e$ $v_r=5$	${}^3P^o$ $v_b=1$	1999.01	2.923[-5]
${}^3D^e$ $v_r=2$	${}^3P^o$ $v_b=1$	1996.19	2.870[-5]
${}^{1,5}P^o$ $v_r=0$	${}^{1,5}D^e$ $v_r=1$	100.62	2.129[-5]
${}^3S^e$ $v_r=1$	${}^3P^o$ $v_r=2$	59.81	1.859[-5]
${}^{1,5}P^o$ $v_r=1$	${}^{1,5}D^e$ $v_r=1$	111.94	1.842[-5]
${}^{1,5}P^o$ $v_r=0$	${}^{1,5}D^e$ $v_b=0$	2063.73	1.713[-5]
${}^3D^e$ $v_r=0$	${}^3F^o$ $v_r=1$	88.83	1.703[-5]
${}^{1,5}P^o$ $v_r=0$	${}^{1,5}D^e$ $v_r=2$	41.90	1.639[-5]
${}^3S^e$ $v_r=2$	${}^3P^o$ $v_r=1$	126.26	1.597[-5]
${}^3D^e$ $v_r=1$	${}^3P^o$ $v_r=0$	204.31	1.480[-5]
${}^3D^e$ $v_r=1$	${}^3P^o$ $v_b=0$	2216.43	1.394[-5]
${}^3D^e$ $v_r=3$	${}^3P^o$ $v_b=1$	1998.04	1.382[-5]
${}^3D^e$ $v_r=0$	${}^3P^o$ $v_r=2$	51.09	1.313[-5]
${}^{1,5}P^o$ $v_r=0$	${}^{1,5}S^e$ $v_r=2$	52.84	1.235[-5]
${}^{1,5}F^o$ $v_r=0$	${}^{1,5}G^e$ $v_r=1$	72.90	1.155[-5]
${}^{1,5}P^o$ $v_r=0$	${}^{1,5}S^e$ $v_r=1$	115.15	1.151[-5]
${}^{1,5}F^o$ $v_r=0$	${}^{1,5}D^e$ $v_r=2$	46.85	1.144[-5]
${}^3D^e$ $v_r=1$	${}^3P^o$ $v_r=1$	122.74	1.119[-5]
${}^3D^e$ $v_r=1$	${}^3F^o$ $v_r=1$	99.37	1.118[-5]
${}^3D^e$ $v_r=0$	${}^3P^o$ $v_r=1$	112.20	1.089[-5]

Although the Υ_{RB} for the other resonance states is less than those of these two states by one order of magnitude, the transition that results in a shallow-bound state ($J_f=1, v_b=1$) tends to exhibit relatively high transition rates.

Figure 15 illustrates the resonance-to-bound transition lines with the branching ratio into the bound state Υ_{RB} . The resonance states exhibiting high Υ_{RB} values have binding energies of over a few eV outside of the energy range where the Vesman mechanism Eq. (2) occurs. How-

TABLE III. Resonance energies, decay rates into continuum ($\Gamma_{\text{RC}(-)}$, $\Gamma_{\text{RC}(+)}$, and $\Gamma_{\text{RC}} = \Gamma_{\text{RC}(-)} + \Gamma_{\text{RC}(+)}$) and decay rates into other resonance or bound states ($\Gamma_{\text{RB}+\text{RR}'}$) are listed. The uncertainty in parentheses is determined by the difference between the velocity and length gauge calculations. The decay rates with † are obtained solely from the velocity-gauge calculation. The notation $x[y]$ represents $x \times 10^y$.

Symmetry	v_r	$E_{J,v_r}^{(R)}$ (m.a.u.)	ε_{J,v_r} (eV)	$\Gamma_{\text{RC}(-)}$ (ps^{-1})	$\Gamma_{\text{RC}(+)}$ (ps^{-1})	Γ_{RC} (ps^{-1})	$\Gamma_{\text{RB}} + \Gamma_{\text{RR}'}$ (ps^{-1})
$1,^5S^e$	0	-0.1570992	218.1111		7.95[-2]	7.95(13)[-2]	-
$1,^5S^e$	1	-0.1423772	135.2785		6.97[-2]	6.97(14)[-2]	-
$1,^5S^e$	2	-0.1313023	72.9662		6.36[-2]	6.36(17)[-2]	-
$1,^5S^e$	3	-0.1240038	31.9011		6.10[-2]	6.10(24)[-2]	-
$1,^5S^e$	4	-0.1205763	12.6165		6.15[-2]	6.15(10)[-2]	3.413(2)[-7]
$1,^5S^e$	5	-0.1192779	5.3112		6.15[-2]	6.15(3)[-2]	1.676(1)[-7]
$1,^5S^e$	6	-0.1187383	2.2750		6.15[-2]	6.15(1)[-2]	7.477(5)[-8]
$1,^5S^e$	7	-0.1185083	0.9810		6.23[-2]	6.23(1)[-2]	3.251(2)[-8]
$1,^5S^e$	8	-0.1184093	0.4241		5.52[-2]	5.52†[-2]	1.405(1)[-8]
$^3P^o$	0	-0.1559995	211.9236	2.96[-2]	4.87[-2]	7.84(17)[-2]	-
$^3P^o$	1	-0.1415010	130.3486	2.61[-2]	4.29[-2]	6.89(23)[-2]	-
$^3P^o$	2	-0.1306392	69.2351	2.38[-2]	3.95[-2]	6.32(19)[-2]	-
$^3P^o$	3	-0.1235815	29.5255	2.29[-2]	3.82[-2]	6.12(18)[-2]	-
$^3P^o$	4	-0.1203769	11.4945	2.29[-2]	3.85[-2]	6.13(4)[-2]	3.540(1)[-7]
$^3P^o$	5	-0.1191823	4.7732	2.23[-2]	3.84[-2]	6.07(5)[-2]	1.736(1)[-7]
$^3P^o$	6	-0.1186922	2.0157	2.05[-2]	3.84[-2]	5.88(4)[-2]	7.696(1)[-8]
$^3P^o$	7	-0.1184862	0.8567	1.70[-2]	3.89[-2]	5.59(28)[-2]	3.321(1)[-8]
$^3P^o$	8	-0.1183988	0.3650	1.31[-2]	4.08[-2]	5.39†[-2]	1.421(1)[-8]
$1,^5D^e$	0	-0.1538540	199.8521	3.65[-2]	3.97[-2]	7.61(22)[-2]	-
$1,^5D^e$	1	-0.1397954	120.7520	3.23[-2]	3.51[-2]	6.74(29)[-2]	-
$1,^5D^e$	2	-0.1293582	62.0277	2.97[-2]	3.27[-2]	6.24(24)[-2]	-
$1,^5D^e$	3	-0.1227887	25.0647	2.90[-2]	3.20[-2]	6.10(24)[-2]	-
$1,^5D^e$	4	-0.1200140	9.4526	2.95[-2]	3.23[-2]	6.18(10)[-2]	3.31(3)[-7]
$1,^5D^e$	5	-0.1190108	3.8085	2.97[-2]	3.22[-2]	6.19(9)[-2]	1.602(1)[-7]
$1,^5D^e$	6	-0.1186110	1.5590	2.98[-2]	3.16[-2]	6.18(21)[-2]	6.92(2)[-8]
$1,^5D^e$	7	-0.1184481	0.6421	3.02[-2]	2.98[-2]	6.18†[-2]	2.90(1)[-8]
$^3F^o$	0	-0.1507635	182.4632	3.93[-2]	3.37[-2]	7.29(24)[-2]	-
$^3F^o$	1	-0.1373475	106.9787	3.50[-2]	3.01[-2]	6.51(38)[-2]	-
$^3F^o$	2	-0.1275472	51.8380	3.26[-2]	2.86[-2]	6.11(26)[-2]	-
$^3F^o$	3	-0.1217280	19.0964	3.24[-2]	2.84[-2]	6.08(17)[-2]	-
$^3F^o$	4	-0.1195513	6.8493	3.35[-2]	2.85[-2]	6.20(1)[-2]	2.240(1)[-7]
$^3F^o$	5	-0.1187990	2.6166	3.37[-2]	2.85[-2]	6.22(34)[-2]	1.025(1)[-7]
$^3F^o$	6	-0.1185143	1.0147	3.42[-2]	2.83[-2]	6.24†[-2]	4.14(1)[-8]
$^3F^o$	7	-0.1184043	0.3957	3.59[-2]	2.78[-2]	6.38†[-2]	1.640(1)[-8]
$^3S^e$	0	-0.1220939	21.1551		5.77[-2]	5.77(7)[-2]	5.733(1)[-3]
$^3S^e$	1	-0.1200073	9.4149		6.18[-2]	6.18(29)[-2]	4.217(1)[-4]
$^3S^e$	2	-0.1190591	4.0801		6.13[-2]	6.13(6)[-2]	4.692(1)[-4]
$^3S^e$	3	-0.1186477	1.7656		6.13[-2]	6.13(6)[-2]	1.694(1)[-4]
$^3S^e$	4	-0.1184698	0.7645		6.10[-2]	6.10(7)[-2]	7.337(1)[-5]
$^3S^e$	5	-0.1183928	0.3311		4.59[-2]	4.59†[-2]	3.173(1)[-5]
$1,^5P^o$	0*	-0.1223588	22.6458	4.83[-2]	3.36[-2]	8.19(26)[-2]	4.004(1)[-2]
$1,^5P^o$	0	-0.1219101	20.1211	2.37[-2]	3.94[-2]	6.31(24)[-2]	1.854(1)[-4]
$1,^5P^o$	1	-0.1198988	8.8046	2.35[-2]	3.85[-2]	6.20(14)[-2]	5.371(1)[-5]
$1,^5P^o$	2	-0.1190018	3.7575	2.21[-2]	3.83[-2]	6.04(8)[-2]	2.714(1)[-5]
$1,^5P^o$	3	-0.1186187	1.6023	1.98[-2]	3.83[-2]	5.81(8)[-2]	1.275(1)[-5]
$1,^5P^o$	4	-0.1184554	0.6837	1.55[-2]	3.90[-2]	5.45(7)[-2]	5.780(1)[-6]
$1,^5P^o$	5	-0.1183858	0.2918	1.25[-2]	3.92[-2]	5.17†[-2]	2.557(1)[-6]
$^3D^e$	0	-0.1215586	18.1432	2.86[-2]	3.16[-2]	6.01(19)[-2]	3.501(1)[-3]
$^3D^e$	0*	-0.1201091	9.9880	1.83[-2]	4.03[-2]	5.87(26)[-2]	5.766(1)[-2]
$^3D^e$	1	-0.1196858	7.6061	2.92[-2]	3.36[-2]	6.28(16)[-2]	3.306(1)[-4]
$^3D^e$	2	-0.1188932	3.1468	2.97[-2]	3.23[-2]	6.21(5)[-2]	4.979(1)[-5]
$^3D^e$	3	-0.1185649	1.2993	2.98[-2]	3.21[-2]	6.19(3)[-2]	2.276(1)[-5]
$^3D^e$	4	-0.1184294	0.5369	2.89[-2]	3.20[-2]	6.09(6)[-2]	1.016(1)[-5]
$1,^5F^o$	0	-0.1210306	15.1726	3.60[-2]	2.76[-2]	6.36(11)[-2]	4.2(1)[-5]
$1,^5F^o$	1	-0.1194050	6.0264	3.50[-2]	2.80[-2]	6.30(12)[-2]	2.803(5)[-5]
$1,^5F^o$	2	-0.1187524	2.3547	3.46[-2]	2.80[-2]	6.27(8)[-2]	1.357(7)[-5]
$1,^5F^o$	3	-0.1184976	0.9210	3.46[-2]	2.81[-2]	6.27(14)[-2]	6.07(5)[-6]
$1,^5F^o$	4	-0.1183980	0.3604	3.55[-2]	2.83[-2]	6.38(9)[-2]	2.55(3)[-6]

TABLE IV. Several states of $dd\mu^*$ and $dt\mu^*$ that have a high branching ratio resulting in a bound state muonic molecule. The total angular momentum and the vibrational quantum number of the bound state are denoted as J_f and v_b , respectively. E_γ denotes the monoenergetic x-ray energy.

Symmetry	v_r	$E_{J,v_r}^{(R)}$ (m.a.u.)	ε_{J,v_r} (eV)	Γ_{RC} (ps $^{-1}$)	J_f	v_b	E_γ (eV)	Γ_{RB} (ps $^{-1}$)	Υ_{RB}
$dd\mu^*$									
$^3D^e$	0^*	-0.120 109	9.9880	5.87[-2]	1	1	1989.35	5.62[-2]	0.49
$^{1,5}P^o$	0^*	-0.122 359	22.6458	8.19[-2]	0	1	2010.56	3.51[-2]	0.30
$^3S^e$	0	-0.122 094	21.1551	5.77[-2]	1	1	1978.18	5.66[-3]	0.09
$^3D^e$	0	-0.121 559	18.1432	6.01[-2]	1	1	1981.19	3.44[-3]	0.05
$dt\mu^*$									
D	7	-0.121 778	7.369	7.62[-2]	1	1	2026.72	2.68[-2]	0.35
P	4	-0.123 874	19.160	9.51[-2]	0	1	2049.10	2.50[-2]	0.26
S	0	-0.159 195	217.887	7.14[-2]	1	1	1816.19	3.01[-3]	0.04
D	1	-0.156 357	201.927	7.37[-2]	1	1	1832.16	2.79[-3]	0.04
D	5	-0.122 998	14.231	6.14[-2]	1	1	2019.85	1.39[-3]	0.02

ever, the $^{1,5}P^o$ ($v_r = 0^*$) states of $dd\mu^*$ and the $P(v_r = 4)$ state of $dt\mu^*$ have a binding energy ε_{J,v_r} greater than 15.4 eV, i.e., they could be produced by Auger transitions from the shallower resonance states formed by the Vesman mechanism. Future research should comprise an investigation into the target conditions and laser-assisted processes that efficiently produce these resonance states.

IV. CONCLUSION

We comprehensively studied the radiative decay of $dd\mu^*$ in the resonance states. Using the complex coordinate rotation method, the x-ray spectra from the decay into a continuum were calculated. We determined the characteristic shape of the spectra that depends on the rovibrational states of the resonance states of $dd\mu$. We highlighted that the orbital angular momentum according to the relative motion of the decay fragments clearly affects the x-ray spectrum. For resonance states with a non-zero total orbital angular momentum $J > 0$, the J -increasing and decreasing decay results in broadening of the x-ray spectrum. A quantitative analysis compared with the adiabatic approximation showed that non-adiabatic effects are remarkable in the kinetic energy

distribution of the decay fragments. The radiative decay rates into the bound state were also calculated, and the branching ratios against the radiative decay into the continuum were revealed. We found that some states of $dd\mu^*$ and $dt\mu^*$ demonstrate significantly high branching ratios into the bound state, which introduces a direct pathway for producing muonic molecules and may contribute to the acceleration of μCF cycles.

The x-ray spectra obtained in this study can be used when they are measured in a future precise x-ray spectroscopy experiment and provide a fundamental understanding of muonic molecular dynamics.

ACKNOWLEDGMENTS

We are grateful to S. Okada and Y. Toyama (Chubu University, Japan) for the detection of the x-ray spectra using TES microcalorimeter. T.Y. is thankful for the financial support received from the Japan Society for the Promotion of Science (JSPS) KAKENHI Grant No. JP24K06911. Y.K. is thankful for the JSPS KAKENHI Grant No. JP24K00549.

This work was partly achieved using the supercomputer systems at Hokkaido University and Kyushu University.

-
- | | |
|---|--|
| <p>[1] W. H. Breunlich, P. Kammel, J. S. Cohen, and M. Leon, <i>Annu. Rev. Nucl. Part. Sci.</i> 39, 311 (1989).</p> <p>[2] L. I. Ponomarev, <i>Contemp. Phys.</i> 31, 219 (1990).</p> <p>[3] H. E. Rafelski, D. Harley, G. R. Shin, and J. Rafelski, <i>Journal of Physics B: Atomic, Molecular and Optical Physics</i> 24, 1469 (1991).</p> <p>[4] P. Froelich, <i>Adv. Phys.</i> 41, 405 (1992).</p> <p>[5] J. S. Cohen, Capture of negative exotic particles by atoms, ions and molecules, <i>Reports on Progress in Physics</i> 67, 1769 (2004).</p> <p>[6] P. Froelich and J. Wallenius, Resonance sidepath in muon catalyzed fusion, <i>Phys. Rev. Lett.</i> 75, 2108 (1995).</p> | <p>[7] J. Wallenius and P. Froelich, Formation of metastable $dt\mu$ molecules in $t\mu(2s) - D_2$ collisions, <i>Phys. Rev. A</i> 54, 1171 (1996).</p> <p>[8] Y. Kino and M. Kamimura, <i>Hyperfine Interactions</i> 101, 191 (1996).</p> <p>[9] V. N. Pomerantsev and V. P. Popov, Coulomb deexcitation of pionic hydrogen within the close-coupling method, <i>Phys. Rev. A</i> 73, 040501 (2006).</p> <p>[10] V. P. Popov and V. N. Pomerantsev, Formation and collisional quenching of the long-lived $2s$ state of muonic hydrogen, <i>Phys. Rev. A</i> 83, 032516 (2011).</p> <p>[11] V. P. Popov and V. N. Pomerantsev, Collision-induced</p> |
|---|--|

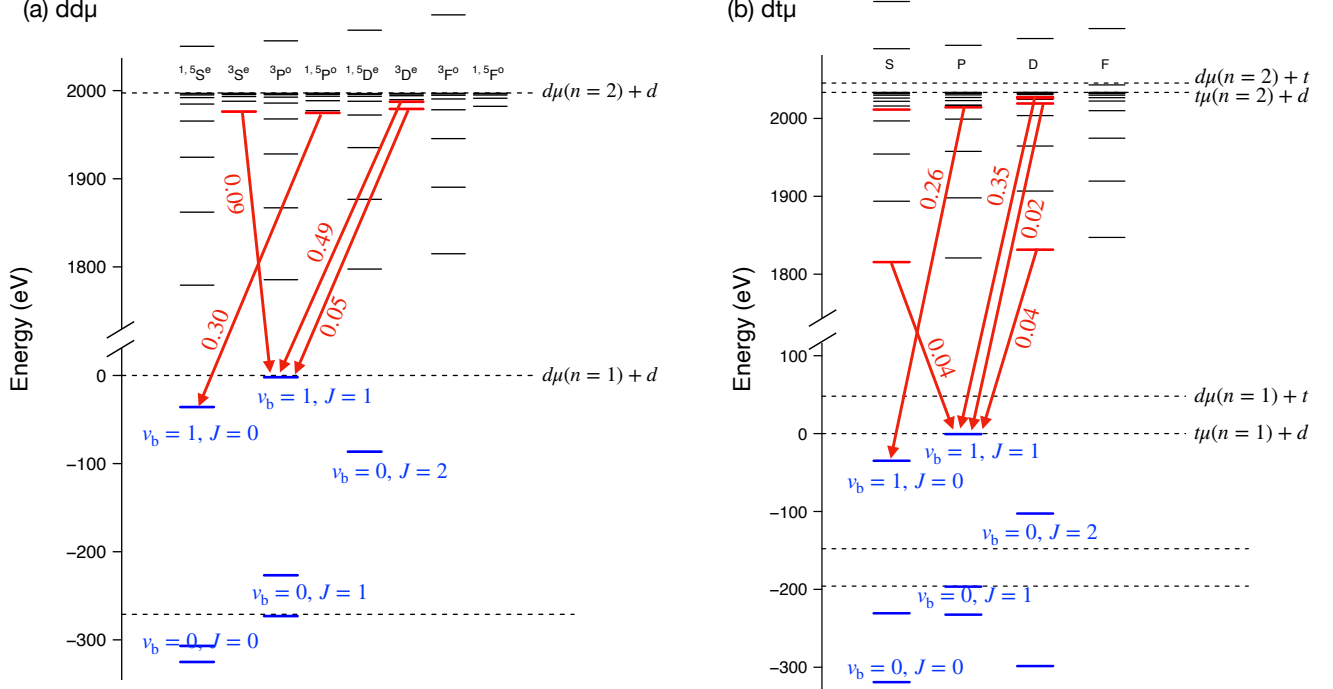


FIG. 15. Energy diagram of resonance and bound energy levels for (a) $dd\mu$ and (b) $dt\mu$. The red arrows highlight the transitions with a high branching ratio into the bound state.

radiative quenching and other disintegration modes of the $2s$ state of muonic hydrogen and deuterium atoms, Phys. Rev. A **105**, 042804 (2022).

- [12] T. Yamashita, Y. Kino, K. Okutsu, S. Okada, and M. Sato, Roles of resonant muonic molecule in new kinetics model and muon catalyzed fusion in compressed gas, Scientific Reports **12**, 6393 (2022).
- [13] R. Pohl, H. Daniel, F. J. Hartmann, P. Hauser, Y. W. Liu, F. Kottmann, C. Maierl, V. E. Markushin, M. Mühlbauer, C. Petitjean, W. Schott, and D. Taqqu, Observation of the molecular quenching of $m\mu(2s)$ atoms, Hyperfine Interactions **138**, 35 (2001).
- [14] R. Pohl, H. Daniel, F. J. Hartmann, P. Hauser, F. Kottmann, V. E. Markushin, M. Mühlbauer, C. Petitjean, W. Schott, D. Taqqu, and P. Wojciechowski-Grosshauser, Observation of long-lived muonic hydrogen in the $2s$ state, Phys. Rev. Lett. **97**, 193402 (2006).
- [15] L. Ludhova, F. D. Amaro, A. Antognini, F. Biraben, J. M. R. Cardoso, C. A. N. Conde, A. Dax, S. Dhawan, L. M. P. Fernandes, T. W. Hänsch, V. W. Hughes, P. Indelicato, L. Julien, P. E. Knowles, F. Kottmann, Y.-W. Liu, J. A. M. Lopes, C. M. B. Monteiro, F. Mulhauser, F. Nez, R. Pohl, P. Rabinowitz, J. M. F. dos Santos, L. A. Schaller, C. Schwob, D. Taqqu, and J. F. C. A. Veloso, Phys. Rev. A **75**, 040501 (2007).
- [16] M. Diepold, F. D. Amaro, A. Antognini, F. m. c. Biraben, J. a. M. R. Cardoso, D. S. Covita, A. Dax, S. Dhawan, L. M. P. Fernandes, A. Giesen, A. L. Gouvea, T. Graf, T. W. Hänsch, P. Indelicato, L. Julien, C.-Y. Kao, P. Knowles, F. Kottmann, E.-O. Le Bigot, Y.-W. Liu, J. A. M. Lopes, L. Ludhova, C. M. B. Monteiro, F. m. c. Mulhauser, T. Nebel, F. m. c. Nez, P. Rabinowitz, J. M. F. dos Santos, L. A. Schaller, K. Schuhmann, C. Schwob, D. Taqqu, J. a. F. C. A. Veloso, J. Vogelsang, and R. Pohl, Phys. Rev. A **88**, 042520 (2013).
- [17] E. A. Vesman, ZhETF Pisma Redaktsiui **5**, 113 (1967).
- [18] E. Lindroth, J. Wallenius, and S. Jonsell, Decay rates of excited muonic molecular ions, Phys. Rev. A **68**, 032502 (2003).
- [19] S. Kilic, J.-P. Karr, and L. Hilico, Phys. Rev. A **70**, 042506 (2004).
- [20] S. Okada, T. Azuma, D. A. Bennett, P. Caradonna, W. B. Doriese, M. S. Durkin, J. W. Fowler, J. D. Gard, T. Hashimoto, R. Hayakawa, G. C. Hilton, Y. Ichinohe, P. Indelicato, T. Isobe, S. Kanda, M. Katsuragawa, N. Kawamura, Y. Kino, Y. Miyake, K. M. Morgan, K. Ninomiya, H. Noda, G. C. O'Neil, T. Okumura, C. D. Reintsema, D. R. Schmidt, K. Shimomura, P. Strasser, D. S. Swetz, T. Takahashi, S. Takeda, S. Takeshita, H. Tatsuno, Y. Ueno, J. N. Ullom, S. Watanabe, and S. Yamada, J. Low Temp. Phys. **200**, 445 (2020).
- [21] T. Okumura, T. Azuma, D. A. Bennett, P. Caradonna, I. Chiu, W. B. Doriese, M. S. Durkin, J. W. Fowler, J. D. Gard, T. Hashimoto, R. Hayakawa, G. C. Hilton, Y. Ichinohe, P. Indelicato, T. Isobe, S. Kanda, Y. Kato, M. Katsuragawa, N. Kawamura, Y. Kino, M. K. Kubo, K. Mine, Y. Miyake, K. M. Morgan, K. Ninomiya, H. Noda, G. C. O'Neil, S. Okada, K. Okutsu, T. Osawa, N. Paul, C. D. Reintsema, D. R. Schmidt, K. Shimomura, P. Strasser, H. Suda, D. S. Swetz, T. Takahashi, S. Takeda, S. Takeshita, M. Tampo, H. Tatsuno, X. M. Tong, Y. Ueno, J. N. Ullom, S. Watanabe, and S. Yamada, Phys. Rev. Lett. **127**, 053001 (2021).
- [22] T. Okumura, T. Azuma, D. A. Bennett, I. Chiu, W. B.

- Doriese, M. S. Durkin, J. W. Fowler, J. D. Gard, T. Hashimoto, R. Hayakawa, G. C. Hilton, Y. Ichinohe, P. Indelicato, T. Isobe, S. Kanda, M. Katsuragawa, N. Kawamura, Y. Kino, K. Mine, Y. Miyake, K. M. Morgan, K. Ninomiya, H. Noda, G. C. O'Neil, S. Okada, K. Okutsu, N. Paul, C. D. Reintsema, D. R. Schmidt, K. Shimomura, P. Strasser, H. Suda, D. S. Swetz, T. Takahashi, S. Takeda, S. Takeshita, M. Tampo, H. Tatsuno, Y. Ueno, J. N. Ullom, S. Watanabe, and S. Yamada, Proof-of-principle experiment for testing strong-field quantum electrodynamics with exotic atoms: High precision x-ray spectroscopy of muonic neon, *Phys. Rev. Lett.* **130**, 173001 (2023).
- [23] E. Hiyama, Y. Kino, and M. Kamimura, *Progress in Particle and Nuclear Physics* **51**, 223 (2003).
- [24] P. J. Mohr and B. N. Taylor, CODATA Recommended Values of the Fundamental Physical Constants: 1998, *Journal of Physical and Chemical Reference Data* **28**, 1713 (1999), https://pubs.aip.org/aip/jpr/article-pdf/28/6/1713/12118344/1713_1_online.pdf.
- [25] E. Tiesinga, P. J. Mohr, D. B. Newell, and B. N. Taylor, CODATA Recommended Values of the Fundamental Physical Constants: 2018*, *Journal of Physical and Chemical Reference Data* **50**, 033105 (2021), https://pubs.aip.org/aip/jpr/article-pdf/doi/10.1063/5.0064853/16697641/033105_1_online.pdf.
- [26] D. A. Varshalovich, A. N. Moskalev, and V. K. Khersonskii, *Quantum Theory of Angular Momentum* (World Scientific, Singapore, 1988).
- [27] T. N. Rescigno and V. McKoy, *Phys. Rev. A* **12**, 522 (1975).
- [28] Y. Ho, *Physics Reports* **99**, 1 (1983).
- [29] A. Buchleitner, B. Gremaud, and D. Delande, *Journal of Physics B: Atomic, Molecular and Optical Physics* **27**, 2663 (1994).
- [30] T. Yamashita, E. Hiyama, D. Yoshida, and M. Tachikawa, Spontaneous radiative dissociation of the second bound state of positronium hydride, *Phys. Rev. A* **105**, 012814 (2022).
- [31] S. Hara and T. Ishihara, *Phys. Rev. A* **40**, 4232 (1989).
- [32] A. U. Hazi and H. S. Taylor, Stabilization method of calculating resonance energies: Model problem, *Phys. Rev. A* **1**, 1109 (1970).
- [33] J. Simons, Resonance state lifetimes from stabilization graphs, *The Journal of Chemical Physics* **75**, 2465 (1981), https://pubs.aip.org/aip/jcp/article-pdf/75/5/2465/11123812/2465_1_online.pdf.
- [34] V. A. Mandelshtam, T. R. Ravuri, and H. S. Taylor, Calculation of the density of resonance states using the stabilization method, *Phys. Rev. Lett.* **70**, 1932 (1993).